SIR: Multi-view Inverse Rendering with Decomposable Shadow for Indoor Scenes

Xiaokang Wei[1,2], Zhuoman Liu[1], Yan Luximon[1,2*]

[1]The Hong Kong Polytechnic University,
[2]Laboratory for Artificial Intelligence in Design, HKSAR

{xiaokang.wei,zhuo-man.liu}@connect.polyu.hk, yan.luximon@polyu.edu.hk

Abstract

We propose SIR, an efficient method to decompose differentiable shadows for inverse rendering on indoor scenes using multi-view data, addressing the challenges in accurately decomposing the materials and lighting conditions. Unlike previous methods that struggle with shadow fidelity in complex lighting environments, our approach explicitly learns shadows for enhanced realism in material estimation under unknown light positions. Utilizing posed HDR images as input, SIR employs an SDF-based neural radiance field for comprehensive scene representation. Then, SIR integrates a shadow term with a three-stage material estimation approach to improve SVBRDF quality. Specifically, SIR is designed to learn a differentiable shadow, complemented by BRDF regularization, to optimize inverse rendering accuracy. Extensive experiments on both synthetic and real-world indoor scenes demonstrate the superior performance of SIR over existing methods in both quantitative metrics and qualitative analysis. The significant decomposing ability of SIR enables sophisticated editing capabilities like free-view relighting, object insertion, and material replacement.

1. Introduction

Inverse rendering, a crucial concept in computer graphics and vision, involves deducing scene properties such as geometry, lighting, and materials from images. This process, which inverts the traditional rendering pipeline, has broad applications [1, 2, 3, 4] ranging from photo-realistic editing to augmented reality. The objective is to achieve a high level of realism and accuracy, facilitating a flawless blend of existing scene elements with newly introduced components or properties. However, the complexity inherent in scenes, especially regarding lighting and material attributes, poses significant challenges.

The first challenge lies in the representation of scene geometry and lighting. **i)** For geometry, ranging from conven-
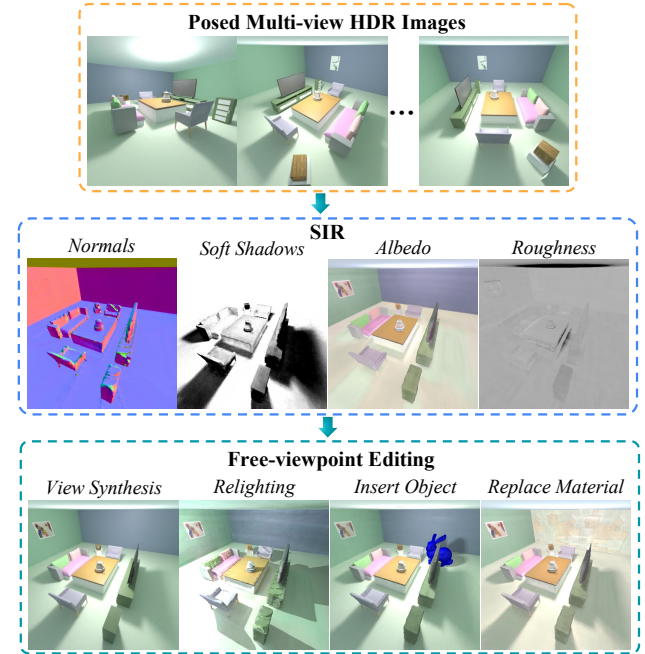

Figure 1. The general pipeline and components of our method. Given a set of posed multi-view HDR images of an indoor scene, **SIR** successfully disentangle the scene appearance into 3D neural fields of shape, global and spatially-varying illumination, soft shadows, and SVBRDFs, which can produce convincing results for several applications such as novel view synthesis, free-viewpoint relighting, object insertion, and material replacement.

tional explicit representations like point clouds and meshes to recent developments in implicit representations, such as neural radiance fields (NeRFs) [5] and DeepSDF [6], vary in their efficiency and computational demands. The fidelity of the yielded scene geometry directly influences the success of inverse rendering approaches. **ii)** For lighting, the choice between low dynamic range (LDR) [7, 8] and high dynamic range (HDR) [9, 10] fields significantly affects the outcome of the rendering. The former is more computationally efficient, while the latter enables accurate measurements of scene radiance from a collection of photographs with varying

---

*Corresponding author

exposures [11].

The second challenge lies in material estimation, specifically in the decomposition of shadow and albedo. Shadows are highly prevalent and noticeable in indoor scenes because of the primary light sources and the intricate geometric occlusions between objects. This necessitates the decomposition of shadows to achieve realistic effects in scene editing applications. Existing multi-view methods for indoor scenes have not yet effectively resolved this problem. NVDIFFREC [12] tends to bake pre-existing shadows into the learned albedo results. Such deprecated shadows in their albedo results can lead to inaccurate rendering during editing. For example, if the scene is illuminated by a light source placed at a different position, the shadows they produce cannot shift accordingly as expected. Another inverse rendering method [8] proposes a single-view inverse rendering method to effectively decompose shadows. However, it relies on supervision with direct shading, excluding shadow effects, which are not available in real-world scenes. A self-supervised shadow decomposition approach [13] is proposed, yet it struggles with the challenge of unknown light source locations. Consequently, accurately estimating shadows without explicit supervision and with unknown light sources remains a significant challenge.

In response to these challenges, we propose **SIR** (**S**hadow **I**nverse **R**endering) (see Fig. 1), an innovative inverse rendering method that efficiently decomposes differentiable shadows for indoor scenes without explicit supervision. To address the challenges in representing accurate geometry and detailed lighting, SIR employs an SDF-based neural radiance field for comprehensive scene representation and leverages multi-view HDR images to significantly provide more information for lighting. Then, to overcome the difficulty in decomposing shadows without supervision, we propose a three-stage material estimation process, including *albedo initialization with hard shadows*, *differentiable shadow optimization*, and *instance-level BRDF regularization*. This approach not only elevates SVBRDF quality but also facilitates sophisticated editing capabilities, such as free-view relighting, object insertion, and material replacement. In summary, the main contributions of this work include:

- We propose SIR, a new inverse rendering framework to effectively handle complex indoor scenes.

- We present a novel shadow term that, for the first time, decomposes shadow and albedo in multi-view indoor scenes.

- We present a three-stage material estimation strategy, incorporating differentiable shadow and BRDF regularization.

- Our method exhibits superior inverse rendering accuracy over current methods on both synthetic and real-world indoor scene datasets. Additionally, its robust-

ness is further demonstrated through successful scene editing.

2. Related Works

2.1. Neural Scene Representations

Recent progress in neural scene representations has enhanced the recovery of scene geometry and radiance for inverse rendering tasks. Neural radiance field (NeRF) [5] employs a single Multilayer Perceptron (MLP) to process a 5D light field, thereby learning the radiance field for generating new viewpoints. However, the geometric accuracy of NeRF for inverse rendering is constrained due to the inherent ambiguity in volume rendering [14]. To address this, methods like NeuS [15] and VolSDF [16] have been developed, transforming Signed Distance Functions (SDF) [6] into densities for more accurate volume rendering. In addition to these implicit approaches, explicit representation methods [17, 18] have also been proposed to accelerate the rendering process. Among them, DMTet [19] and other DMTet-based solutions [12, 20] utilize a differentiable marching tetrahedral layer to refine surface meshes. Recently, many neural scene representations have been proposed with hybrid methods such as InstantNGP [21] and 3D Gaussian [22], which significantly improve the efficiency and reduce the computational cost. However, these methods often struggle to accurately capture the complex topologies and small-scale structures found in indoor scenes. To effectively reconstruct the geometry of indoor environments, we propose an optimization of topology, lighting, and materials using an SDF-based neural radiance field.

2.2. Lighting Estimation

In the field of inverse rendering, accurately estimating lighting, particularly in indoor scenes, is a complex and essential task. Most current illumination estimation methods operate on single images, with a primary emphasis on integrating virtual objects into real images rather than making substantial alterations to the scene's illumination [23, 24, 25]. While traditional methods like a single environment map [26, 27] and spherical lobes [28] have been used, they often neglect spatial variations and high-frequency details in lighting. Recent innovations [9, 29] have attempted to improve 3D lighting representation, but still grapple with challenges like spatial instability and the lack of HDR information. A per-pixel spatially-varying spherical Gaussians (SVSG) lighting representation [30] is proposed to capture high-frequency effects and demonstrate that SGs are superior to spherical harmonics (SH) for depicting lighting details in indoor scenes. Neural-PIL [31] proposes a pre-integrated lighting network based on image-based lighting (IBL), showing better performances on conveying global illumination than SGs and SH. Hence, in our method, we utilize a neural
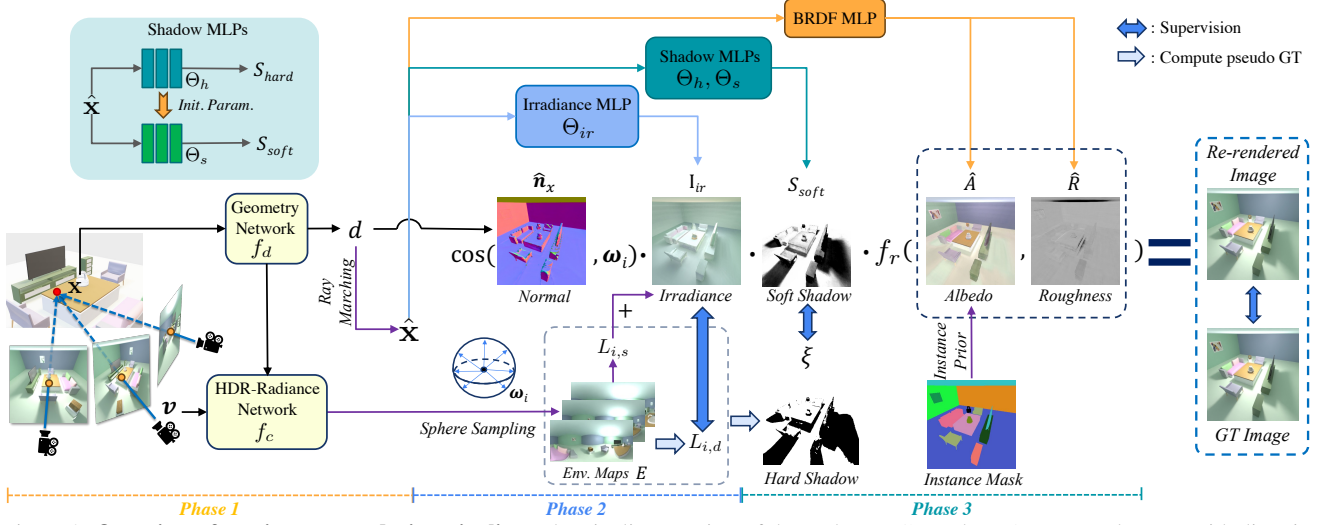
Figure 2. **Overview of our inverse rendering pipeline.** The pipeline consists of three phases: 1) In phase 1, we sample a ray with direction $\boldsymbol{v}$ and spatial point $\mathbf{x}$ from the given posed HDR images. The geometry network f_d learns the signed distance d, and the HDR-radiance network f_c learns radiance $\hat{C}$. Ray marching is then employed to obtain the surface point $\hat{\mathbf{x}}$. 2) In phase 2, we sample diffuse incoming light $L_{i,d}$ from environment maps E for learning irradiance I_{ir}. We also calculate the specular incoming light $L_{i,s}$ and the pseudo hard shadow ξ. 3) In phase 3, hard shadow S_{hard} is learned using Θ_h with pseudo ground truth. We then initialize the parameters of Θ_s using the optimized parameters of Θ_h. Instance-level BRDF regularizers are applied, and the whole rendering equation is optimized to update the soft shadow S_{soft}, albedo $\hat{A}$, and roughness $\hat{R}$.

outgoing HDR field to represent the IBL at any spatial point, thereby ensuring a more accurate and detailed depiction of indoor lighting scenarios with a focus on physically accurate HDR lighting prediction.

2.3. Material Estimation

Material estimation in inverse rendering can be categorized into two levels: object level and scene level. Object-level estimation [12, 32, 33, 34, 35] focuses on individual objects, often in controlled or simplified environments. Object-level approaches are generally less complex, as they deal with fewer variables and more straightforward lighting conditions. In contrast, scene-level material estimation [36, 37] is significantly more challenging due to the complexity and variability of entire scenes. This includes diverse lighting, multiple objects with different materials, and shadows.

The complexity of scene-level material estimation is further compounded by the choice between single-view and multi-view approaches. Single-view material estimation [26, 30], despite its simplicity and lower data requirements, often faces the ill-posed issue, where insufficient information leads to ambiguous or inaccurate estimations. This is particularly evident in complex scenes where a single viewpoint cannot capture the entirety of the scene's lighting and material properties. In contrast, multi-view material estimation [12, 32, 33, 36] leverages images from multiple viewpoints, providing a more comprehensive understanding of the scene. It can significantly reduce the ambiguity associated with single-view estimations, allowing for more

accurate and reliable material property extraction. Our work utilizes multi-view images for material estimation, specifically addressing the challenges at the scene level.

The rendering equation. The traditional rendering equation [38] is formulated following the principles of energy conservation in physics. It computes the outgoing radiance value L_o at surface point $\hat{\mathbf{x}}$ with surface normal $\hat{\boldsymbol{n}}_x$ along view direction $\boldsymbol{\omega}_o$ by integrating over the hemisphere $\Omega^+ = \{\boldsymbol{\omega}_i : \boldsymbol{\omega}_i \cdot \hat{\boldsymbol{n}}_x > 0\}$, where $\boldsymbol{\omega}_i$ is the incident light direction:

$$L_o(\hat{\mathbf{x}}, \boldsymbol{\omega}_o) = \int_{\Omega^+} L_i(\hat{\mathbf{x}}, \boldsymbol{\omega}_i) f_r(\hat{\mathbf{x}}, \boldsymbol{\omega}_i, \boldsymbol{\omega}_o)(\boldsymbol{\omega}_i \cdot \hat{\boldsymbol{n}}_x) \mathrm{d}\boldsymbol{\omega}_i \quad (1)$$

The function $L_i(\hat{\mathbf{x}}, \boldsymbol{\omega}_i)$ represents the incoming radiance at the surface point $\hat{\mathbf{x}}$ from $\boldsymbol{\omega}_i$, while the BRDF function f_r quantifies the proportion of light arriving from direction $\boldsymbol{\omega}_i$ that is reflected in the direction $\boldsymbol{\omega}_o$ at point $\hat{\mathbf{x}}$.

3. Methods

3.1. Overview

Given a set of posed HDR images of an indoor scene captured under static illumination, our method aims to accurately recover the geometry, global spatially-varying illumination, shadows, and Bidirectional Reflectance Distribution Functions (SVBRDFs), which can be used in editing applications such as free-view relighting and insert objects with accurate shadow. We represent global and spatially varying illumination and geometry as an HDR neural radiance

field with SDF, and we utilize MLPs to represent an irradiance field (Sec. 3.2). To handle the ambiguity between shadows and albedo of indoor scenes well, we introduce the hard shadow term based on the HDR neural radiance field, and we propose a shadow field to represent the continuous shadow (Sec. 3.3). To eliminate residual shadow and efficiently improve the quality of SVBRDFs, we present a three-stage material estimation strategy with differentiable shadow and BRDF regularization (Sec. 3.4). The overview of our method is illustrated in Fig. 2.

3.2. Geometry and Lighting Representaion

Neural radiance fields (NeRFs) [5] can use simple MLPs to represent the continuous 3D scene geometry and appearance. Guided by the rendering equation, physically-based shading models rely on high-quality reconstructed geometry. However, the density-based NeRF's recovered geometry has not achieved satisfactory results. Motivated by the effectiveness of SDF-based NeRF [15, 16], our method employs VolSDF [16] as the backbone to represent our geometry and radiance field. It is noted that alternative SDF-based NeRF variants are also applicable [39, 40, 41]. In particular, we replace the LDR input of VolSDF with HDR images because HDR contains richer environmental lighting information. The attributes of a 3D scene, including SDF and HDR-radiance, are parameterized by a *geometry network* f_d and an *HDR-radiance network* f_c by:

$$d = f_d(\mathbf{x}), \quad \mathbf{c} = f_c(\mathbf{x}, \boldsymbol{v}) \qquad (2)$$

where the geometry network f_d maps a spatial position $\mathbf{x}$ to its signed distance to the surface and the HDR-radiance network f_c predict HDR radiance value conditioned on position $\mathbf{x}$ and view direction $\boldsymbol{v}$. To render a pixel, we utilize volume rendering similar to NeRF [5], which accumulates the density σ from SDF and radiance $\mathbf{c}$ along the view direction $\boldsymbol{v}$ of ray $\mathbf{r}$ by:

$$\hat{C}(\mathbf{r}) = \sum_{i=1}^{P} T_i \alpha_i \mathbf{c}_i \qquad (3)$$

where $T_i = \exp(-\sum_{j=1}^{i-1} \sigma_j \delta_j)$ and $\alpha_i = 1 - \exp(-\sigma_i \delta_i)$ denote the transmittance and alpha value of sampled point, respectively. δ_i is the distance between neighboring sampled points. P is the number of sampled points along a ray. σ_i and $\mathbf{c}_i$ are predicted attributes by the HDR-radiance network f_c. Following VolSDF [16], we transform SDF value d to density σ by [16]:

$$\sigma(\mathbf{x}) = \begin{cases} \frac{1}{\beta}\left(1 - \frac{1}{2}\exp\left(\frac{f_d(\mathbf{x})}{\beta}\right)\right), & \text{if } f_d(\mathbf{x}) < 0, \\ \frac{1}{2\beta}\exp\left(-\frac{f_d(\mathbf{x})}{\beta}\right), & \text{if } f_d(\mathbf{x}) \geq 0, \end{cases} \qquad (4)$$

where β is a learnable parameter to control the sparsity near the surface. Following this parameterization, we can get

a high quality smooth surface from the zero level-set of predicted SDF $d_\Omega(\mathbf{x})$ of the space $\Omega \in \mathbb{R}^3$, and surface normal can be computed as the gradient of the predicted SDF w.r.t. surface point $\hat{\mathbf{x}}$, *i.e.*, $\hat{\boldsymbol{n}}_x = \frac{\nabla d_\Omega(\hat{\mathbf{x}})}{\|\nabla d_\Omega(\hat{\mathbf{x}})\|}$.

We adopt image-based lighting to represent scene environment lighting, which can deal with direct and indirect lighting conditions well. Inspired by InvRender [33], we obtain spatially-varying environment map $E \in \mathbb{R}^{3 \times H \times W}$ at any position of an indoor scene derived from the pre-trained outgoing HDR radiance field. According to the rendering equation, the environment incoming lighting $L_i(\mathbf{x})$ at a spatial position $\mathbf{x}$ is obtained by querying the environment map E:

$$L_i(\mathbf{x}) = \int_{\Omega^+} E(\mathbf{x}, \boldsymbol{\omega}_i)(\boldsymbol{\omega}_i \cdot \boldsymbol{n}_x)\mathrm{d}\boldsymbol{\omega}_i, \qquad (5)$$

$$E(\mathbf{x}, \boldsymbol{\omega}_i) = \hat{C}(\mathbf{p}_x, -\boldsymbol{\omega}_i) \qquad (6)$$

where $\boldsymbol{\omega}_i$ is the incident light direction, $\mathbf{p}_x$ is the intersection position with scene surface along a ray starting from $\mathbf{x}$ with a direction $-\boldsymbol{\omega}_i$ by ray tracing, the incoming lighting at position $\mathbf{x}$ is the integrate of radiance along any $\boldsymbol{\omega}_i$ over hemisphere Ω^+. We use a simple convolution operation on an environment map E to calculate diffuse lighting $L_{i,d}$ at any spatial position $\mathbf{x}$, and Monte Carlo Path Tracing to obtain the specular lighting $L_{i,s}$.

We introduce the irradiance field by using an MLP $\Theta_{ir}(\mathbf{x})$ to represent the irradiance I_{ir} at any input 3D location $\mathbf{x}$, which can efficiently model a compact and continuous spatially varying and global illumination of indoor scenes under complex lighting conditions. The *irradiance field* $I_{ir}(\mathbf{x}) = \Theta_{ir}(\mathbf{x})$ is supervised by $L_{i,d}(\mathbf{x})$, which is derived from the outgoing HDR radiance field. Here, utilizing arbitrary spatial positions as inputs, instead of restricting to object surface points, allows for capturing a continuous and spatially varied lighting environment. This strategy is particularly advantageous for applications that involve inserting objects into a scene, as it ensures accurate global illumination across any point in the space. Therefore, the irradiance MLP can effectively simulate realistic lighting conditions, offering consistent and precise illumination regardless of the object's placement within the environment. It can also significantly enhance the fidelity of the lighting model in complex spatial applications.

3.3. Hard Shadow Estimation

Shadow term depicts the occlusion between geometry and environment lighting. The phenomenon of cast shadow is significant in indoor scenes where the primary light source is relatively strong, and we note that gradient optimization tends to bake shadows into the albedo [20]. To enable high-quality relighting, we first consider separating hard shadows from scenes to avoid ambiguity with albedo in material estimation. The traditional graphics method using ray marching

can directly calculate the hard shadow term according to the relationship between the main light and geometry if the light location and geometry are known. However, formulating the shadow term is still a challenging problem due to the unknown location of the light source.

According to the HDR radiance attribute, HDR can save more accurate radiance value without cut-off compared LDR, and HDR intensity of the main light is much greater than the environment light. Here, we assume that if the incident light intensity from any direction at a spatial point is lower than an intensity threshold, the point will be considered in a hard shadow area, which means $\xi(\mathbf{x}) = 0$. Therefore, we propose a simple strategy to address the hard shadow estimation under the unknown location of the light source derived from the prior HDR radiance field (Sec. 3.2). Formally:

$$\xi(\mathbf{x}) = \begin{cases} 1, & \text{if } \Gamma_{max}(\mathbf{x}) \geq \mu, \\ 0, & \text{if } \Gamma_{max}(\mathbf{x}) < \mu, \end{cases} \quad (7)$$

$$\Gamma_{max}(\mathbf{x}) = \max_i \Gamma_i(\mathbf{x}, \boldsymbol{\omega}_i), \text{where } i = 1, 2, ..., N \quad (8)$$

where Γ_i is incoming radiance intensity at spatial position $\mathbf{x}$ along $\boldsymbol{\omega_i}$, which is the sum of radiance $E(\mathbf{x}, \boldsymbol{\omega}_i)$ (along the RGB channel). N is the number of sample rays. μ is the threshold that can distinguish HDR radiance intensity between the main light and environment light. We introduce a shadow field by using an MLP $\Theta_h(\mathbf{x})$ to represent the hard shadow S_{hard} at any input 3D location $\mathbf{x}$, which can efficiently model compactness and continuous hard shadow distribution under unknown light location condition.

The *hard shadow field* $S_{hard}(\mathbf{x}) = \Theta_h(\mathbf{x})$ is supervised by $\xi(\mathbf{x})$, which caches the shadow distribution for an indoor scene to avoid duplicate computation during material estimation. Meanwhile, the hard shadow field can provide the initial shadow value to ensure the accurate gradient flow of material.

3.4. BRDF

Physically Based Rendering (PBR) provides a more accurate representation of how light interacts with material properties [42, 43]. We adopt the physically-based microfacet BRDF model of Unreal Engine [43] to approximate the surface reflectance property and introduce a BRDF MLP f_r to model the albedo and roughness of the scene. However, directly optimizing such a BRDF model can easily lead to non-convergence of roughness, due to the insufficient distribution of viewpoints in the training set as well as self-occlusion issues [33]. Moreover, shadows are prone to be inadvertently baked into the albedo [12] during direct optimization. We observed that the decomposition processes of albedo and shadow are more closely related to the diffuse component, while the specular component primarily influences the roughness. Based on our observations, we propose

a *three-stage* material estimation strategy to alleviate this ambiguity problem.

Inspired by [44] and [12], we leverage the Monte Carlo rendering algorithm and image-based lighting representation to recover albedo $\hat{A}$, roughness $\hat{R}$, and soft shadow $\hat{S}$. The rendering equation Eq. 1 can be written as:

$$L_o(\hat{\mathbf{x}}, \boldsymbol{\omega}_o) = \int_{\Omega^+} E(\hat{\mathbf{x}}, \boldsymbol{\omega}_i)(\frac{\hat{A}_x}{\pi} + f_s(\hat{\mathbf{x}}, \boldsymbol{\omega}_i, \boldsymbol{\omega}_o))(\boldsymbol{\omega}_i \cdot \hat{\boldsymbol{n}}_x)\mathrm{d}\boldsymbol{\omega}_i \quad (9)$$

$$= L_{o,d}(\hat{\mathbf{x}}) + L_{o,s}(\hat{\mathbf{x}}, \boldsymbol{\omega}_o) \quad (10)$$

where $\hat{\boldsymbol{n}}_x$ is the normal at a surface point $\hat{\mathbf{x}}$; $\boldsymbol{\omega}_i$ is light incident direction; $\boldsymbol{\omega}_o$ is view direction; f_s is the specular BRDF term at the surface point based on the Microfacet model. Further, we represent the rendering result with two components for learning, where $L_{o,d}$ is the diffuse component and $L_{o,s}$ is the specular component. The detailed formulation can be found in Sec. A of the Appendix.

Stage 1: Albedo initialization with S_{hard}. We adopt the diffuse component based on the Lambertian model [38] to optimize coarse albedo $\hat{A}$ predicted by f_r. Here, we introduce a hard shadow term at the initial phase of gradient optimization, specifically to prevent the encroachment of hard shadows into the albedo in dimly lit areas. This strategic inclusion is pivotal for maintaining and elevating the accuracy of the albedo, ensuring that the intrinsic coloration of surfaces is faithfully rendered without the distortion of shadow artifacts. Then, we optimize the initial albedo from diffuse component $L_{o,d}(\hat{\mathbf{x}})$ by utilizing estimated diffuse lighting E (Sec. 3.2) and hard shadow ξ (Sec. 3.3):

$$L_{o,d}(\hat{\mathbf{x}}) = \frac{\hat{A}_x}{\pi} \xi(\hat{\mathbf{x}}) \int_{\Omega^+} E(\hat{\mathbf{x}}, \boldsymbol{\omega}_i)(\boldsymbol{\omega}_i \cdot \hat{\boldsymbol{n}}_x)\mathrm{d}\boldsymbol{\omega}_i \quad (11)$$

Note that we have pre-computed the *irradiance* and *hard shadow* terms using respective MLPs Θ_{ir} and Θ_h to represent, which can effectively minimize the number of unnecessary ray samples in the material estimation process, thereby enhancing computational efficiency, so we can write the diffuse component integral as:

$$L_{o,d}(\hat{\mathbf{x}}) = \frac{\hat{A}_x}{\pi} S_{hard}(\hat{\mathbf{x}}) I_{ir}(\hat{\mathbf{x}}) \quad (12)$$

where $\hat{\mathbf{x}}$ is the surface point, which is the intersection point along the camera ray. The spatially varying illumination and hard shadow are first queried from irradiance field Θ_{ir} and hard shadow field Θ_s.

Stage 2: Differentiable shadow optimization. In stage 1, we incorporated a hard shadow, leading to a coarse albedo approximation. However, this method struggles with capturing detailed shadows, largely because the binary nature of the hard shadow field oversimplified the light-shadow

interaction. This simplification, combined with shadow detail depending on ray sampling density, can not effectively represent the nuanced intensity of soft shadows, especially those affected by changes in light source intensity and object placement. We tackle this problem by introducing a differentiable soft shadow $S_{soft}(\mathbf{x})$ using an MLP to represent the *soft shadow field* $\Theta_s(\mathbf{x})$, which is designed to provide a more nuanced representation of shadows, extending beyond the binary constraints of the hard shadow field. Crucially, the initial parameters of this soft shadow field Θ_s are inherited from the hard shadow field Θ_h. We simply replace the hard shadow with the differentiable soft shadow in Eq. 12, and update the predicted soft shadow by optimizing the diffuse radiance:

$$L_{o,d}(\hat{\mathbf{x}}) = \frac{\hat{A}_x}{\pi} S_{soft}(\hat{\mathbf{x}}) I_{ir}(\hat{\mathbf{x}}) \qquad (13)$$

Stage 3: Instance-level BRDF regularization. We note that lighting and materials are inherently entangled in rendered images, posing a challenge for their complete separation. This can lead to ambiguities during optimization, where elements of lighting could be inaccurately attributed to the albedo. To alleviate the ambiguity, we propose a novel albedo regularizer $\mathcal{L}_{albedo}$. We assume that the luminance of the albedo is uniformly distributed at the instance level, showing no luminance variations. Formally:

$$\mathcal{L}_{albedo} = \Big| \sum_{i=1}^{K} (\hat{A} - \Phi_{inv}(\frac{\sum_p \Phi(\hat{A}) \odot M_i}{\sum_p M_i})) \Big| \qquad (14)$$

$$\mathcal{L}_{rough} = \Big| \sum_{i=1}^{K} (\hat{R} - \frac{\sum_p \hat{R} \odot M_i}{\sum_p M_i}) \Big| \qquad (15)$$

where $\Phi(\cdot)$ is an operator to obtain the *V* value in HSV color domain by converting RGB-space to HSV-space, $\Phi_{inv}(\cdot)$ is an inverse operator to convert HSV-space to RGB-space [20], M_i is the prior instance segmentation mask, K denotes the instance classes of the indoor scene, p denotes the minibatch of 3D points, and $\odot$ denotes an element-wise product. Meanwhile, we introduce a roughness smooth regularization $\mathcal{L}_{rough}$, which constrains the roughness value on the same instance level to be similar.

3.5. Training

We optimize the geometry, spatially varying illumination, shadow, and SVBRDF of the indoor scenes in ***three phases***: 1) training of geometry and HDR radiance field, 2) training of hard shadow and irradiance field, 3) training of BRDF with soft shadow field.

Phase 1: Training of geometry and HDR radiance field. We train the geometry network f_d and the HDR-radiance network f_c in an end-to-end manner using the following loss [16]:

$$\mathcal{L}_1 = \mathcal{L}_{recon} + \lambda_{eik}\mathcal{L}_{eik} + \lambda_{normal}\mathcal{L}_{normal}, \qquad (16)$$

where $\mathcal{L}_{recon} = \sum_{\mathbf{r} \in R} ||\hat{C}(\mathbf{r}) - C(\mathbf{r})||_1$, R denotes the set of rays samples in the minibatch, $\hat{C}$ is the volume rendering results in Eq. 3, C is the ground truth color. $\mathcal{L}_{recon}$ use ℓ_1 to minimize the difference between each pixel's predicted radiance and its ground-truth radiance. $\mathcal{L}_{eik}$ is an eikonal term [16] to regularize the gradients of geometry network formulated as:

$$\mathcal{L}_{eik} = \sum_{\mathbf{x} \in \mathcal{X}} (||\nabla d(\mathbf{x})||_2 - 1)^2, \qquad (17)$$

where $\mathcal{X}$ is the minibatch of 3D points uniformly sampled in 3D space and nearby surface. $\mathcal{L}_{normal}$ is a normal smooth loss [45], which constrains the predicted normals $\boldsymbol{n}_i$ connected to the sampled density gradient normals $\bar{\boldsymbol{n}}_i$ along the ray. Formally:

$$\mathcal{L}_{normal} = \sum_i T_i \alpha_i ||\boldsymbol{n}_i - \bar{\boldsymbol{n}}_i||^2 \qquad (18)$$

where T_i is the transmittance value and α_i is the alpha value of the ith sample along the ray, as defined in Eq. 3.

Phase 2: Training of hard shadow and irradiance field. In Sec. 3.2 and Sec. 3.3, we can obtain the incoming diffuse lighting $L_{i,d}$ and hard shadow ξ, which serve as the ground truth for supervising the predicted irradiance I_{ir} and hard shadow S_{hard} via ℓ_1 loss.

$$\mathcal{L}_2 = ||L_{i,d}(\hat{\mathbf{x}}) - I_{ir}(\hat{\mathbf{x}})||_1 + ||\xi(\hat{\mathbf{x}}) - S_{hard}(\hat{\mathbf{x}})||_1 \quad (19)$$

Phase 3: Training of BRDF and soft shadow field. During the optimization of intrinsic decomposition, we adopt a multi-stage training scheme to train BRDF and soft shadow field to avoid the ambiguity between albedo and shadow. We first train the initial albedo under shadow and roughness layer parameters fixed, then we train the albedo and shadow with $\mathcal{L}_{albedo}$ under roughness layer parameters fixed, and we finetune the roughness with $\mathcal{L}_{rough}$ after the albedo and shadow MLP have been trained.

$$\mathcal{L}_3 = \mathcal{L}_{render} + \lambda_{albedo}\mathcal{L}_{albedo} + \lambda_{rough}\mathcal{L}_{rough}, \quad (20)$$

where $\mathcal{L}_{render}$ is $= ||\hat{L}_o(\hat{\mathbf{x}}) - L_o(\hat{\mathbf{x}})||_1$, minimizing the ℓ_1 error between the re-rendered (see Eq. 9) and GT images. More details of the rendering equation can refer to Sec. A and B.1 in the Appendix.

4. Experiments

Our SIR pipeline is validated through experiments conducted on both synthetic and real-world indoor datasets.

4.1. Indoor Datasets

Owing to the absence of shadow effects within the existing HDR multi-view datasets for indoor scenes, we recognize the need for a more robust evaluation of our methodology.

Table 1. Quantitative results for all baselines and ours. All scores are calculated as an average across 6 scenes from the synthetic dataset.

| | Albedo | | | Roughness | Shadow | View Synthesis | | |
	PSNR↑	SSIM ↑	LPIPS ↓	MSE ↓	MSE ↓	PSNR↑	SSIM ↑	LPIPS ↓
NVDIFFREC [12]	16.6377	0.7906	0.3736	0.0531	-	23.8048	0.8606	0.1863
IBL-NeRF [36]	16.7773	0.8468	0.2161	0.0564	-	24.5258	**0.9263**	**0.0844**
PhySG [32]	10.5322	0.7076	0.3838	-	-	26.1667	0.9202	0.1014
InvRender [33]	12.5401	0.6740	0.4935	**0.0412**	-	23.8582	0.7521	0.3923
SIR (Ours)	**20.2767**	**0.8600**	**0.2154**	0.0445	**0.0541**	**28.5456**	0.9258	0.0964

Table 2. Quantitative results for all baselines and ours. All scores are calculated as an average across 2 scenes from the real-world dataset.

| | View Synthesis | | |
	PSNR↑	SSIM ↑	LPIPS ↓
NVDIFFREC [12]	22.7146	0.7798	0.4456
IBL-NeRF [36]	**24.2781**	0.7491	0.5225
PhySG [32]	22.1492	0.7796	0.4581
InvRender [33]	20.1327	0.6694	0.6384
SIR (Ours)	22.8176	**0.8345**	**0.2931**

Consequently, we have developed two distinct inverse rendering datasets tailored specifically for indoor scene evaluation: 1) The synthetic dataset is an extension of the DM-NeRF dataset [46], featuring six indoor scenes. It includes 300 posed images for training and 200 for testing. Each image has 400×400 pixels. We alter the locations and colors of objects within these scenes and enhance various object properties (*e.g.*, albedo, roughness, shadow, instance mask, *etc.*). 2) Our real-world dataset includes two indoor scenes with elaborate materials and sophisticated lighting conditions. Utilizing a professional camera, we capture 120 HDR images for each scene, merging each HDR image from three distinct exposures (from $\frac{1}{15000}$ s to $\frac{1}{8}$ s). The captured images are processed to a resolution of 512×512 pixels, 85% for training and 15% for testing. These two datasets provide challenging indoor scenes for inverse rendering analysis.

4.2. Implementation

All neural fields in our network are implemented by multi-layer perceptrons (MLPs) with ReLU activations. For the geometry network f_d and HDR-radiance network f_c, we follow the default setting from VolSDF [16], where f_d is an 8-layer MLP with hidden dimension 256 and f_c is a 4-layer MLP with hidden dimension 256. The architectures of irradiance MLP, shadow MLPs, and BRDF MLP all contain 4 layers with 256 hidden units. Positional encoding [5] is applied to the input 3D locations and directions with 10 and 4 frequency components, respectively. For the SDF-based neural radiance field, we implement the two networks in PyTorch and optimize using Adam [47] with a learning rate of 5×10^{-4} for 250K iterations. In irradiance and hard shadow estimation, we use the Adam optimizer with a learning rate of 5×10^{-4} for 10K iterations, and we use 512 samples to compute the irradiance (Sec. 3.2) and shadow (Sec. 3.3). In all three stages of material estimation, we use the Adam optimizer with a learning rate of 10^{-3} for 25K iterations, and we use 128 samples to compute the BRDF term (Sec. 3.4). All experiments are conducted on a single NVIDIA GeForce RTX 3090 GPU.

4.3. Inverse Rendering

We select four notable and widely recognized inverse rendering methods as our baselines: 1) NVDIFFREC [12], 2) IBL-NeRF [36], 3) PhySG [32], and 4) InvRender [33]. Specifically, NVDIFFREC employs a DMTet-based approach, utilizing a differentiable marching tetrahedral layer to learn object-level meshes. IBL-NeRF, on the other hand, is a NeRF-based method for inverse rendering. PhySG and InvRender use an SDF-based neural radiance field for inverse rendering, which are both evaluated on object-level datasets. For fair comparisons on indoor scenes, we have minor modifications to adapt these baselines. Specifically, we align the geometric backbone of both InvRender [33] and PhySG [32] with our geometry representation (*i.e.*, VolSDF), considering that both use SDF-based neural radiance fields for geometry. Further details are provided in Sec. B.2 in Appendix.

We report image quality metrics: PSNR, SSIM [48], and LPIPS [49] on test viewpoints for view synthesis results and albedo, as well as the mean squared error (MSE) for roughness and shadow predictions. The evaluations of our method, as evidenced by the quantitative results in Table 1 and qualitative results in Fig. 3, demonstrate that our SIR outperforms existing methods in decomposing material attributes like albedo and roughness, and more notably, in shadow extraction. This leads to superior view synthesis results compared to other methods on indoor scenes. These results convincingly demonstrate the efficiency of the proposed shadow term in enhancing the overall view synthesis. Furthermore, as shown in Table 2 and Fig. 3, our method exhibits a remarkable capability to handle complex lighting conditions in real-world indoor scenes. This ability is crucial for achieving precise and reliable material estimations for inverse rendering.

Table 3. Quantitative results of ablation study on SIR. All scores are calculated as an average across 6 scenes from the synthetic dataset.

	Albedo			Roughness	Shadow	View Synthesis		
	PSNR↑	SSIM ↑	LPIPS ↓	MSE ↓	MSE ↓	PSNR↑	SSIM ↑	LPIPS ↓
(1) w/o S_{hard}, S_{soft}	16.6411	0.8084	0.2919	0.0712	-	28.2254	0.9221	0.0974
(2) w/o S_{soft}	19.3836	0.8052	0.3061	0.0627	0.0650	27.8201	0.8946	0.1897
(3) w/o $\mathcal{L}_{albedo}$	19.2597	0.8454	0.2406	0.0676	0.0863	28.3610	**0.9258**	**0.0924**
Full SIR	**20.2767**	**0.8600**	**0.2154**	**0.0445**	**0.0541**	**28.5456**	**0.9258**	0.0964

4.4. Ablation Study

The key innovation of SIR is the capacity to effectively isolate shadows while ensuring that these shadows are not incorporated into the albedo under an indoor scene. Therefore, this section is dedicated to evaluating the impact of shadow terms, differentiable soft shadow, and albedo regularizer:

(1) Removing shadow terms: Without the shadow terms means removing both S_{hard} in Eq. 12 and S_{soft} in Eq. 13, as well as remove S_{hard} in the training of phase 2 (see Eq. 19). This is to demonstrate the necessity of shadow terms in the rendering equation for accurate inverse rendering.

(2) Removing soft shadow: Without using the differentiable soft shadow S_{soft} in phase 3, the pipeline re-renders images from hard shadows S_{hard} learned in phase 2.

(3) Removing albedo regularizer: This ablation is to evaluate the enhancement of introducing instance-level albedo consistency as a regularizer.

Table 3 (1) clearly shows that removing the shadow term in the rendering equation, leads to a remarkable decline in the performance of novel view synthesis, adversely affecting the albedo estimation as well. The qualitative results in Fig. 4 further indicate that the absence of shadow terms results in incorrect albedo outputs with baked shadows, which then negatively impact the synthesis results. However, intuitively introducing a binary (hard) shadow still leads to suboptimal synthesis as shown in Table 3 (2), particularly noticeable in the inaccuracies around shadow edges (see Fig. 4). Therefore, learning a differentiable soft shadow after an initial hard shadow is necessary to preserve the shadow details in the synthesis images. Moreover, as demonstrated in Table 3 (3), the integration of an instance-level albedo regularizer proves to be effective in maintaining consistency in albedo for each instance, thereby contributing to more accurate synthesis results.

4.5. Scene Editing

Once our SIR has effectively decomposed the intrinsic properties of indoor scenes, it enables the rendering of highly realistic novel view images of edited scenes by altering the values of these individual properties. To evaluate the superior performance of SIR in accurately decomposing intrinsic elements, we have developed the following three distinct editing applications: 1) scene relighting, 2) object insertion, and 3) material replacement.

In Fig. 5, we present the results of editing six varied indoor scenes, encompassing both synthetic and real-world scenarios. The initial row displays the synthesized view images from our test set, serving as the source images for subsequent edits. The second row illustrates the outputs of free-viewpoint relighting experiments, featuring varied light positions and colors. Thanks to the cleanly decomposed albedo, free from any pre-existing shadows, our relighting experiments exhibit new realistic distributions of shadows. The third row is dedicated to object insertion, where we have incorporated six models from the Stanford 3D models [50] into these scenes in diverse positions with different sizes and colors to compare the effect on re-rendering and shadow calculation. Our method achieves realistic shadowing and shading effects for these insertions. Furthermore, the final row shows material replacement: we randomly altered materials within the scenes, experimenting with different textures and levels of roughness (*e.g.*, the wall in the *Bathroom* scene). These convincingly realistic editing results demonstrate the effectiveness and robustness of our SIR in decomposing the intrinsic properties of indoor scenes, which is fundamental for accurate inverse rendering applications.

5. Conclusion

We propose SIR, a multi-view inverse rendering method on indoor scenes, effectively addressing the challenges of material and lighting decomposition by explicitly isolating shadows. Leveraging posed HDR images and an SDF-based neural radiance field, SIR significantly enhances realism in material estimation and scene editing, surpassing previous methods with accurate shadow estimation. The innovative incorporation of a hard shadow term within a three-stage material estimation process substantially improves the quality of SVBRDFs. Extensive evaluations on diverse indoor datasets demonstrate the superiority of SIR in both quantitative and qualitative aspects over existing methods. Note that, since our research primarily addresses the challenge of decomposing shadows and albedo, we directly utilize existing methods for geometric representation. The effectiveness of our approach depends partly on the accuracy of geometric inputs. Therefore, incorporating more precise geometric representations could further improve inverse rendering quality.

Acknowledgement

References

[1] Kaiwen Guo, Peter Lincoln, Philip Davidson, Jay Busch, Xueming Yu, Matt Whalen, Geoff Harvey, Sergio Orts-Escolano, Rohit Pandey, Jason Dourgarian, et al. The relightables: Volumetric performance capture of humans with realistic relighting. *ACM Transactions on Graphics (ToG)*, 38(6):1–19, 2019.

[2] Abhimitra Meka, Maxim Maximov, Michael Zollhoefer, Avishek Chatterjee, Hans-Peter Seidel, Christian Richardt, and Christian Theobalt. Lime: Live intrinsic material estimation. In *Proceedings of the IEEE conference on computer vision and pattern recognition*, pages 6315–6324, 2018.

[3] Julien Philip, Michaël Gharbi, Tinghui Zhou, Alexei A Efros, and George Drettakis. Multi-view relighting using a geometry-aware network. *ACM Trans. Graph.*, 38(4):78–1, 2019.

[4] Abhimitra Meka, Rohit Pandey, Christian Haene, Sergio Orts-Escolano, Peter Barnum, Philip David-Son, Daniel Erickson, Yinda Zhang, Jonathan Taylor, Sofien Bouaziz, et al. Deep relightable textures: volumetric performance capture with neural rendering. *ACM Transactions on Graphics (TOG)*, 39(6):1–21, 2020.

[5] Ben Mildenhall, Pratul P Srinivasan, Matthew Tancik, Jonathan T Barron, Ravi Ramamoorthi, and Ren Ng. Nerf: Representing scenes as neural radiance fields for view synthesis. *Communications of the ACM*, 65(1):99–106, 2021.

[6] Jeong Joon Park, Peter Florence, Julian Straub, Richard Newcombe, and Steven Lovegrove. Deepsdf: Learning continuous signed distance functions for shape representation. In *Proceedings of the IEEE/CVF conference on computer vision and pattern recognition*, pages 165–174, 2019.

[7] Zian Wang, Jonah Philion, Sanja Fidler, and Jan Kautz. Learning indoor inverse rendering with 3d spatially-varying lighting. In *Proceedings of the IEEE/CVF International Conference on Computer Vision*, pages 12538–12547, 2021.

[8] Zhengqin Li, Jia Shi, Sai Bi, Rui Zhu, Kalyan Sunkavalli, Miloš Hašan, Zexiang Xu, Ravi Ramamoorthi, and Manmohan Chandraker. Physically-based editing of indoor scene lighting from a single image. In *European Conference on Computer Vision*, pages 555–572. Springer, 2022.

[9] Pratul P Srinivasan, Ben Mildenhall, Matthew Tancik, Jonathan T Barron, Richard Tucker, and Noah Snavely. Lighthouse: Predicting lighting volumes for spatially-coherent illumination. In *Proceedings of the IEEE/CVF Conference on Computer Vision and Pattern Recognition*, pages 8080–8089, 2020.

[10] Bjoern Haefner, Simon Green, Alan Oursland, Daniel Andersen, Michael Goesele, Daniel Cremers, Richard Newcombe, and Thomas Whelan. Recovering real-world reflectance properties and shading from hdr imagery. In *2021 International Conference on 3D Vision (3DV)*, pages 1075–1084. IEEE, 2021.

[11] Paul Debevec. Rendering synthetic objects into real scenes: Bridging traditional and image-based graphics with global illumination and high dynamic range photography. In *Acm siggraph 2008 classes*, pages 1–10, 2008.

[12] Jacob Munkberg, Jon Hasselgren, Tianchang Shen, Jun Gao, Wenzheng Chen, Alex Evans, Thomas Müller, and Sanja Fidler. Extracting triangular 3d models, materials, and lighting from images. In *Proceedings of the IEEE/CVF Conference on Computer Vision and Pattern Recognition*, pages 8280–8290, 2022.

[13] Junxuan Li and Hongdong Li. Neural reflectance for shape recovery with shadow handling. In *Proceedings of the IEEE/CVF Conference on Computer Vision and Pattern Recognition*, pages 16221–16230, 2022.

[14] Kai Zhang, Gernot Riegler, Noah Snavely, and Vladlen Koltun. Nerf++: Analyzing and improving neural radiance fields. *arXiv preprint arXiv:2010.07492*, 2020.

[15] Peng Wang, Lingjie Liu, Yuan Liu, Christian Theobalt, Taku Komura, and Wenping Wang. Neus: Learning neural implicit surfaces by volume rendering for multi-view reconstruction. *arXiv preprint arXiv:2106.10689*, 2021.

[16] Lior Yariv, Jiatao Gu, Yoni Kasten, and Yaron Lipman. Volume rendering of neural implicit surfaces. *Advances in Neural Information Processing Systems*, 34, 2021.

[17] Yiyi Liao, Simon Donne, and Andreas Geiger. Deep marching cubes: Learning explicit surface representations. In *Proceedings of the IEEE Conference on Computer Vision and Pattern Recognition*, pages 2916–2925, 2018.

[18] Wenzheng Chen, Joey Litalien, Jun Gao, Zian Wang, Clement Fuji Tsang, Sameh Khamis, Or Litany, and

Sanja Fidler. Dib-r++: learning to predict lighting and material with a hybrid differentiable renderer. *Advances in Neural Information Processing Systems*, 34:22834–22848, 2021.

[19] Tianchang Shen, Jun Gao, Kangxue Yin, Ming-Yu Liu, and Sanja Fidler. Deep marching tetrahedra: a hybrid representation for high-resolution 3d shape synthesis. *Advances in Neural Information Processing Systems*, 34:6087–6101, 2021.

[20] Jon Hasselgren, Nikolai Hofmann, and Jacob Munkberg. Shape, light, and material decomposition from images using monte carlo rendering and denoising. *Advances in Neural Information Processing Systems*, 35:22856–22869, 2022.

[21] Thomas Müller, Alex Evans, Christoph Schied, and Alexander Keller. Instant neural graphics primitives with a multiresolution hash encoding. *ACM Transactions on Graphics (ToG)*, 41(4):1–15, 2022.

[22] Bernhard Kerbl, Georgios Kopanas, Thomas Leimkühler, and George Drettakis. 3d gaussian splatting for real-time radiance field rendering. *ACM Transactions on Graphics*, 42(4), 2023.

[23] Kevin Karsch, Varsha Hedau, David Forsyth, and Derek Hoiem. Rendering synthetic objects into legacy photographs. *ACM Transactions on graphics (TOG)*, 30(6):1–12, 2011.

[24] Mathieu Garon, Kalyan Sunkavalli, Sunil Hadap, Nathan Carr, and Jean-François Lalonde. Fast spatially-varying indoor lighting estimation. In *Proceedings of the IEEE/CVF Conference on Computer Vision and Pattern Recognition*, pages 6908–6917, 2019.

[25] Fangneng Zhan, Changgong Zhang, Yingchen Yu, Yuan Chang, Shijian Lu, Feiying Ma, and Xuansong Xie. Emlight: Lighting estimation via spherical distribution approximation. In *Proceedings of the AAAI Conference on Artificial Intelligence*, volume 35, pages 3287–3295, 2021.

[26] Marc-André Gardner, Kalyan Sunkavalli, Ersin Yumer, Xiaohui Shen, Emiliano Gambaretto, Christian Gagné, and Jean-François Lalonde. Learning to predict indoor illumination from a single image. *arXiv preprint arXiv:1704.00090*, 2017.

[27] Chloe LeGendre, Wan-Chun Ma, Graham Fyffe, John Flynn, Laurent Charbonnel, Jay Busch, and Paul Debevec. Deeplight: Learning illumination for unconstrained mobile mixed reality. In *Proceedings of the IEEE/CVF Conference on Computer Vision and Pattern Recognition*, pages 5918–5928, 2019.

[28] Mathieu Garon, Kalyan Sunkavalli, Sunil Hadap, Nathan Carr, and Jean-François Lalonde. Fast spatially-varying indoor lighting estimation. In *Proceedings of the IEEE/CVF Conference on Computer Vision and Pattern Recognition*, pages 6908–6917, 2019.

[29] Shuran Song and Thomas Funkhouser. Neural illumination: Lighting prediction for indoor environments. In *Proceedings of the IEEE/CVF Conference on Computer Vision and Pattern Recognition*, pages 6918–6926, 2019.

[30] Zhengqin Li, Mohammad Shafiei, Ravi Ramamoorthi, Kalyan Sunkavalli, and Manmohan Chandraker. Inverse rendering for complex indoor scenes: Shape, spatially-varying lighting and svbrdf from a single image. In *Proceedings of the IEEE/CVF Conference on Computer Vision and Pattern Recognition*, pages 2475–2484, 2020.

[31] Mark Boss, Varun Jampani, Raphael Braun, Ce Liu, Jonathan Barron, and Hendrik Lensch. Neural-pil: Neural pre-integrated lighting for reflectance decomposition. *Advances in Neural Information Processing Systems*, 34:10691–10704, 2021.

[32] Kai Zhang, Fujun Luan, Qianqian Wang, Kavita Bala, and Noah Snavely. Physg: Inverse rendering with spherical gaussians for physics-based material editing and relighting. In *Proceedings of the IEEE/CVF Conference on Computer Vision and Pattern Recognition*, pages 5453–5462, 2021.

[33] Yuanqing Zhang, Jiaming Sun, Xingyi He, Huan Fu, Rongfei Jia, and Xiaowei Zhou. Modeling indirect illumination for inverse rendering. In *Proceedings of the IEEE/CVF Conference on Computer Vision and Pattern Recognition*, pages 18643–18652, 2022.

[34] Ruofan Liang, Jiahao Zhang, Haoda Li, Chen Yang, Yushi Guan, and Nandita Vijaykumar. Spidr: Sdf-based neural point fields for illumination and deformation. *arXiv preprint arXiv:2210.08398*, 2022.

[35] Mark Boss, Raphael Braun, Varun Jampani, Jonathan T Barron, Ce Liu, and Hendrik Lensch. Nerd: Neural reflectance decomposition from image collections. In *Proceedings of the IEEE/CVF International Conference on Computer Vision*, pages 12684–12694, 2021.

[36] Changwoon Choi, Juhyeon Kim, and Young Min Kim. Ibl-nerf: Image-based lighting formulation of neural radiance fields. *Computer Graphics Forum*, 42:e14929, 2023.

[37] Zhen Li, Lingli Wang, Mofang Cheng, Cihui Pan, and Jiaqi Yang. Multi-view inverse rendering for large-scale real-world indoor scenes. In *Proceedings of the IEEE/CVF Conference on Computer Vision and Pattern Recognition*, pages 12499–12509, 2023.

[38] James T Kajiya. The rendering equation. In *Proceedings of the 13th annual conference on Computer graphics and interactive techniques*, pages 143–150, 1986.

[39] Qiancheng Fu, Qingshan Xu, Yew Soon Ong, and Wenbing Tao. Geo-neus: Geometry-consistent neural implicit surfaces learning for multi-view reconstruction. *Advances in Neural Information Processing Systems*, 35:3403–3416, 2022.

[40] Zhaoshuo Li, Thomas Müller, Alex Evans, Russell H Taylor, Mathias Unberath, Ming-Yu Liu, and Chen-Hsuan Lin. Neuralangelo: High-fidelity neural surface reconstruction. In *Proceedings of the IEEE/CVF Conference on Computer Vision and Pattern Recognition*, pages 8456–8465, 2023.

[41] Lior Yariv, Peter Hedman, Christian Reiser, Dor Verbin, Pratul P Srinivasan, Richard Szeliski, Jonathan T Barron, and Ben Mildenhall. Bakedsdf: Meshing neural sdfs for real-time view synthesis. *arXiv preprint arXiv:2302.14859*, 2023.

[42] Matt Pharr, Wenzel Jakob, and Greg Humphreys. *Physically based rendering: From theory to implementation*. MIT Press, 2023.

[43] Brian Karis and Epic Games. Real shading in unreal engine 4. *Proc. Physically Based Shading Theory Practice*, 4(3):1, 2013.

[44] Jingsen Zhu, Fujun Luan, Yuchi Huo, Zihao Lin, Zhihua Zhong, Dianbing Xi, Rui Wang, Hujun Bao, Jiaxiang Zheng, and Rui Tang. Learning-based inverse rendering of complex indoor scenes with differentiable monte carlo raytracing. In *SIGGRAPH Asia 2022 Conference Papers*, pages 1–8, 2022.

[45] Dor Verbin, Peter Hedman, Ben Mildenhall, Todd Zickler, Jonathan T Barron, and Pratul P Srinivasan. Ref-nerf: Structured view-dependent appearance for neural radiance fields. in 2022 ieee. In *CVF Conference on Computer Vision and Pattern Recognition (CVPR)*, pages 5481–5490, 2022.

[46] Bing Wang, Lu Chen, and Bo Yang. Dm-nerf: 3d scene geometry decomposition and manipulation from 2d images. *arXiv preprint arXiv:2208.07227*, 2022.

[47] Diederik P Kingma and Jimmy Ba. Adam: A method for stochastic optimization. *International conference on learning representations*, 2015.

[48] Tero Karras, Timo Aila, Samuli Laine, and Jaakko Lehtinen. Progressive growing of gans for improved quality, stability, and variation. In *International Conference on Learning Representations*, 2018.

[49] Richard Zhang, Phillip Isola, Alexei A Efros, Eli Shechtman, and Oliver Wang. The unreasonable effectiveness of deep features as a perceptual metric. In *Proceedings of the IEEE conference on computer vision and pattern recognition*, pages 586–595, 2018.

[50] Brian Curless and Marc Levoy. A volumetric method for building complex models from range images. In *Proceedings of the 23rd annual conference on Computer graphics and interactive techniques*, pages 303–312, 1996.

[51] Bruce Walter, Stephen R Marschner, Hongsong Li, and Kenneth E Torrance. Microfacet models for refraction through rough surfaces. In *Proceedings of the 18th Eurographics conference on Rendering Techniques*, pages 195–206, 2007.

[52] Robert L Cook and Kenneth E. Torrance. A reflectance model for computer graphics. *ACM Transactions on Graphics (ToG)*, 1(1):7–24, 1982.

[53] Christophe Schlick. An inexpensive brdf model for physically-based rendering. In *Computer graphics forum*, volume 13, pages 233–246. Wiley Online Library, 1994.

[54] Zehao Yu, Songyou Peng, Michael Niemeyer, Torsten Sattler, and Andreas Geiger. Monosdf: Exploring monocular geometric cues for neural implicit surface reconstruction. *Advances in neural information processing systems*, 35:25018–25032, 2022.

[55] Ainaz Eftekhar, Alexander Sax, Jitendra Malik, and Amir Zamir. Omnidata: A scalable pipeline for making multi-task mid-level vision datasets from 3d scans. In *Proceedings of the IEEE/CVF International Conference on Computer Vision*, pages 10786–10796, 2021.

[56] Samuli Laine, Janne Hellsten, Tero Karras, Yeongho Seol, Jaakko Lehtinen, and Timo Aila. Modular primitives for high-performance differentiable rendering. *ACM Transactions on Graphics (TOG)*, 39(6):1–14, 2020.

[57] Alexander Kirillov, Eric Mintun, Nikhila Ravi, Hanzi Mao, Chloe Rolland, Laura Gustafson, Tete Xiao, Spencer Whitehead, Alexander C Berg, Wan-Yen Lo, et al. Segment anything. *arXiv preprint arXiv:2304.02643*, 2023.

[58] Xiuming Zhang, Pratul P Srinivasan, Boyang Deng, Paul Debevec, William T Freeman, and Jonathan T Barron. Nerfactor: Neural factorization of shape and reflectance under an unknown illumination. *ACM Transactions on Graphics (ToG)*, 40(6):1–18, 2021.
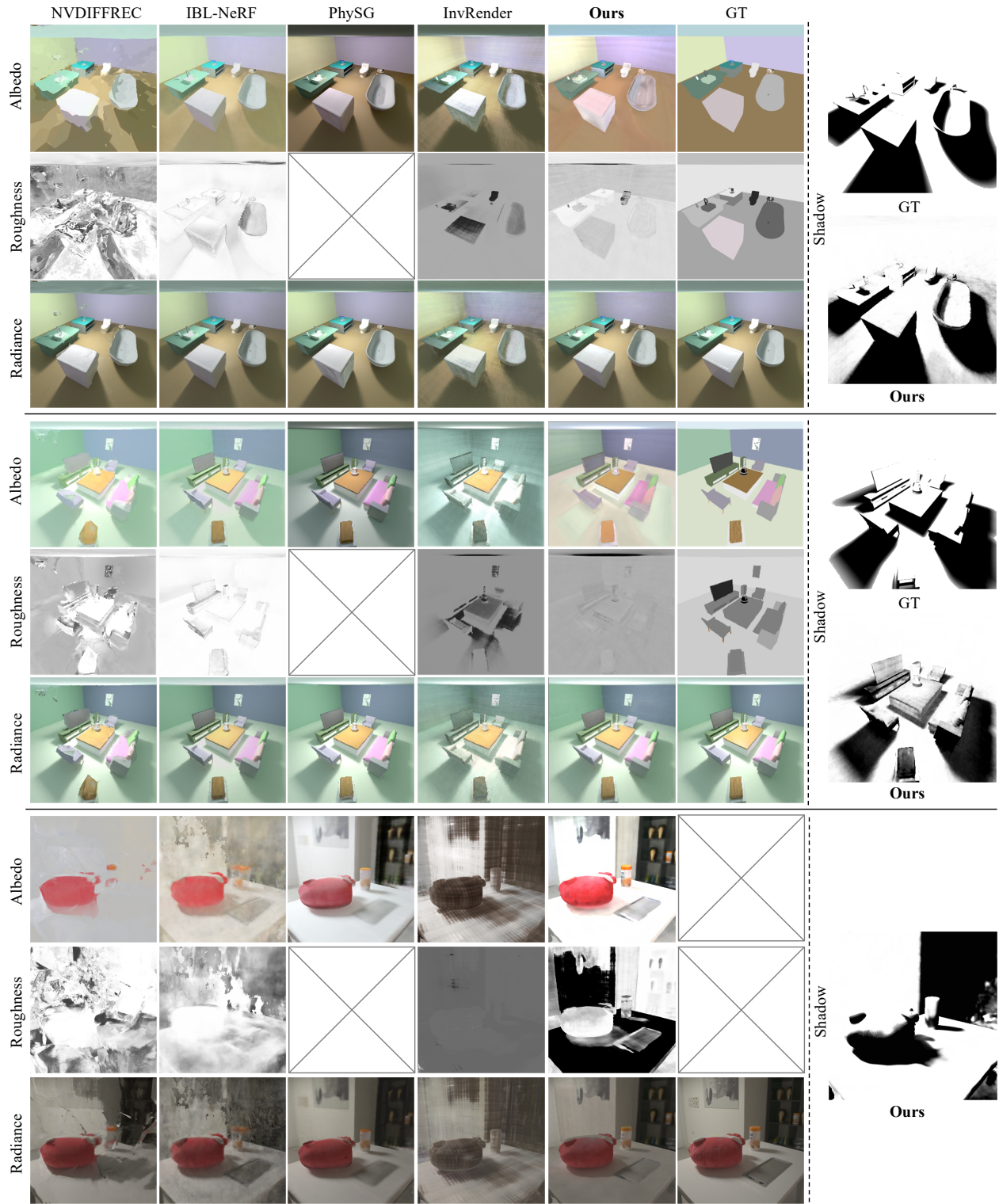
Figure 3. Qualitative results of all methods on two datasets (*Bathroom* and *Restroom* in synthetic dataset, and *Office* in real-world dataset).
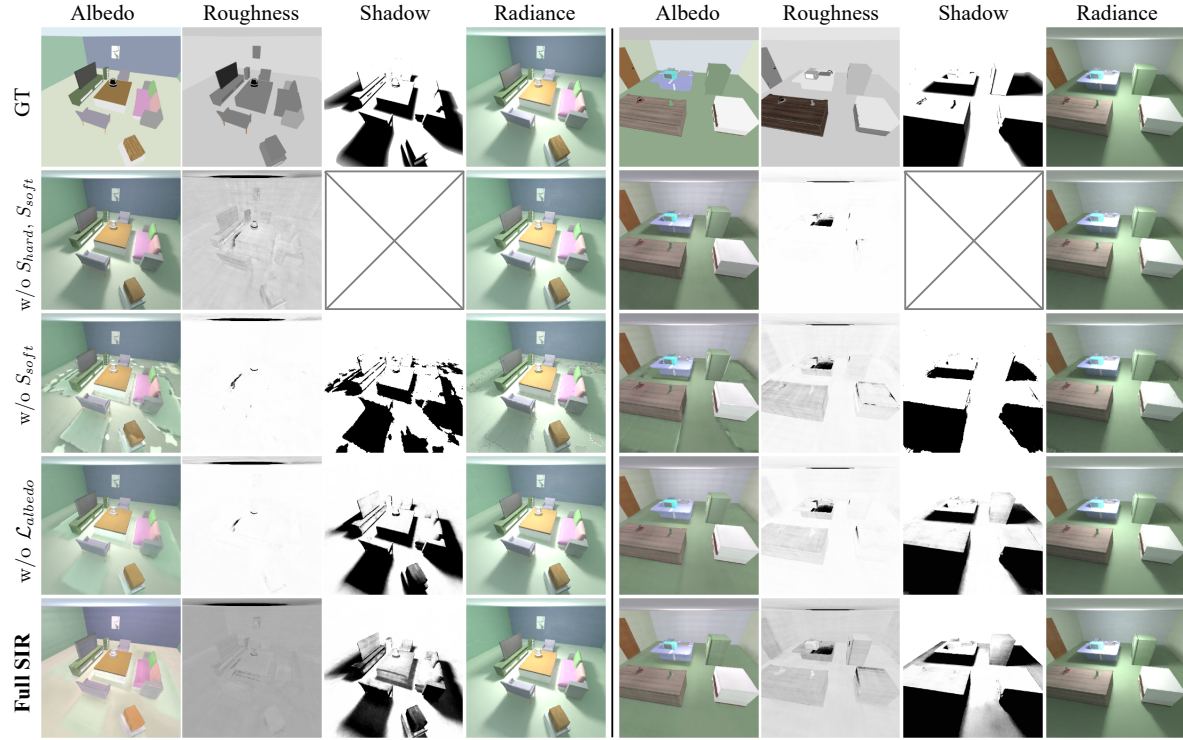
Figure 4. Qualitative results of ablation study on the synthetic dataset (*left: Restroom, right: Kitchen*).
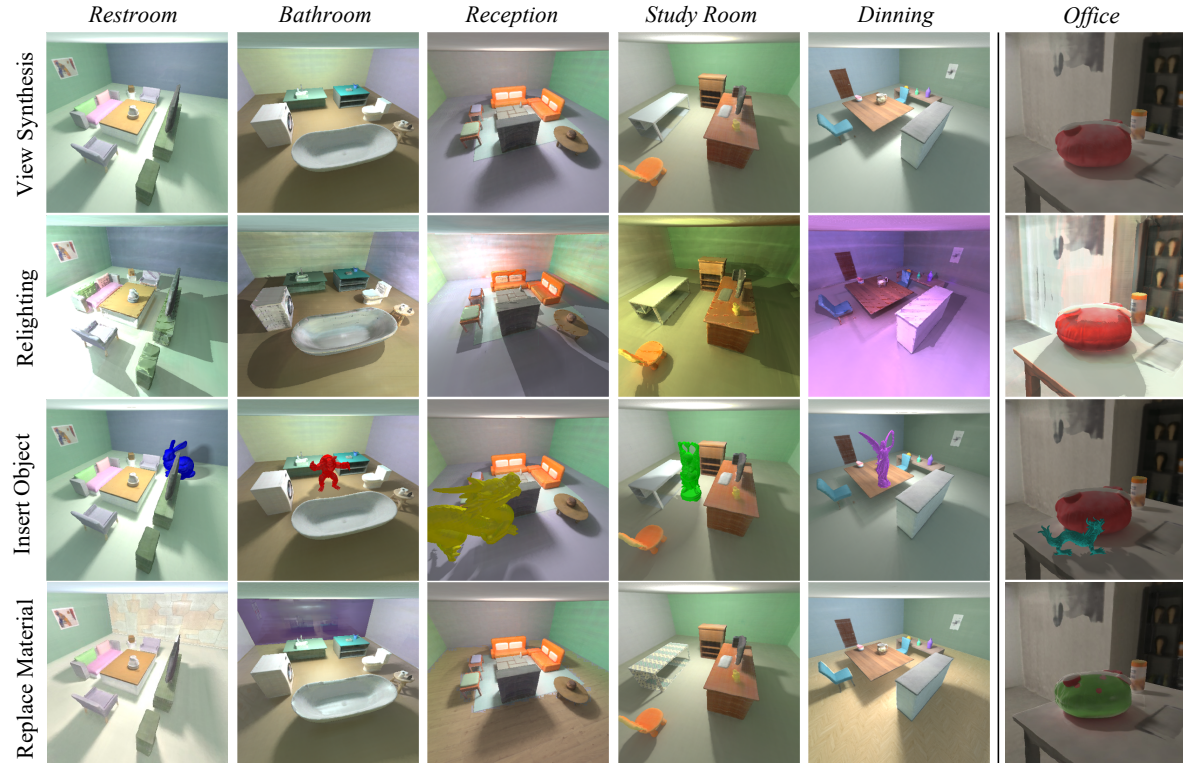

Figure 5. Qualitative results of scene editing using our SIR on the two datasets.

A. BRDF Model

In Sec 3.4, we adapt the Microfacet BRDF model [43, 51] to approximate the surface reflectance property with a set of decomposed intrinsic terms, which can encapsulate the interaction of light with a surface, and the microfacet model provides a robust framework for simulating the reflection from rough surfaces. The BRDF $f_r(\hat{\mathbf{x}}, \boldsymbol{\omega}_i, \boldsymbol{\omega}_o)$ is the ratio between the incoming and outgoing radiance and it is a function of the surface location $\hat{\mathbf{x}}$, incoming direction $\boldsymbol{\omega}_i$, and the outgoing direction $\boldsymbol{\omega}_o$.

$$f_r(\hat{\mathbf{x}}, \boldsymbol{\omega}_i, \boldsymbol{\omega}_o) = f_d(\hat{\mathbf{x}}) + f_s(\hat{\mathbf{x}}, \boldsymbol{\omega}_i, \boldsymbol{\omega}_o) \qquad (21)$$

where $\hat{n}$ is the surface normal at $\hat{\mathbf{x}}$. The BRDF is composed of two terms diffuse reflection f_d and specular reflection f_s. In the 1th stage of BRDF estimation, we use the diffuse reflection term $f_d(\hat{\mathbf{x}}) = \frac{\hat{A}_x}{\pi}$ based on a simple Lambertian model. Here, we introduce the specular BRDF f_s which follows the Cook-Torrance model [52]:

$$f_s = \frac{D(\boldsymbol{h}, \hat{\boldsymbol{n}}, \hat{R}) \cdot F(\boldsymbol{\omega}_o, \boldsymbol{h}) \cdot G(\boldsymbol{\omega}_i, \boldsymbol{\omega}_o, \hat{\boldsymbol{n}}, \hat{R})}{4(\hat{\boldsymbol{n}} \cdot \boldsymbol{\omega}_o)(\hat{\boldsymbol{n}} \cdot \boldsymbol{\omega}_i)} \qquad (22)$$

where $\hat{R}$ is roughness term, $\boldsymbol{h}$ is a half vector, D denotes Normal Distribution Function (NDF), F denotes Fresnel function and G is the Geometry Factor.

The normal distribution function D describes the probability density of microfacet orientations aligned with the half-vector $\boldsymbol{h}$. It is dependent on the macroscopic normal $\boldsymbol{h}$ and the surface roughness $\hat{R}$, influencing the distribution of specular highlights, as follows:

$$D(h) = \frac{\alpha^2}{\pi((\hat{\boldsymbol{n}} \cdot \boldsymbol{h})^2(\alpha^2 - 1) + 1)^2} \qquad (23)$$

where the half-vector $\boldsymbol{h}$ is the normalized vector halfway between the incident light direction and the reflection direction, $\hat{n}$ is the macroscopic surface normal, and α is the surface roughness parameter, ranging from [0,1]. As α approaches 0, the surface tends towards a mirror-like reflection, while α approaching 1 indicates an extremely rough surface.

In the microfacet BRDF model, the Fresnel reflectance term F characterizes the proportion of light reflected from a material's surface at varying angles of incidence. This proportion changes with the angle of incidence, being lowest at normal incidence and highest at grazing angles for non-metallic materials. The Fresnel term can be efficiently computed using Schlick's approximation [53]:

$$F(\boldsymbol{\omega}_o, \boldsymbol{h}) = F_0 + (1 - F_0) \cdot (1 - (\hat{n} \cdot \boldsymbol{h}))^5 \qquad (24)$$

where F_0 is the reflectance at normal incidence, also known as the base reflectance and $\hat{n} \cdot \boldsymbol{h}$ is the dot product between the surface normal and the half-vector, dictating the cosine of

the angle of incidence. In our method, we assume dielectric materials with $F_0 = 0.04$ in the Fresnel term.

In the realm of Physically Based Rendering (PBR), particularly within the context of the GGX Specular reflection model, the Geometry Function G assumes a pivotal role. It is primarily responsible for simulating the occlusion and shadowing effects attributable to the microsurface structure, crucial for accurately rendering light reflections on rough surfaces. The geometry function is typically computed using a combination of the Smith geometry function and the Schlick-GGX approximation. This formula is written as:

$$G(\hat{\boldsymbol{n}}, \boldsymbol{\omega}_o, \boldsymbol{\omega}_i, \alpha) = G_1(\hat{\boldsymbol{n}}, \boldsymbol{\omega}_o, \alpha) \cdot G_1(\hat{\boldsymbol{n}}, \boldsymbol{\omega}_i, \alpha) \qquad (25)$$

Here, G_1 represents the monodirectional shadowing function:

$$G_1(\hat{\boldsymbol{n}}, \boldsymbol{\omega}_o, \alpha) = \frac{\hat{\boldsymbol{n}} \cdot \boldsymbol{\omega}_o}{(\hat{\boldsymbol{n}} \cdot \boldsymbol{\omega}_o)(1 - k) + k} \qquad (26)$$

$$G_1(\hat{\boldsymbol{n}}, \boldsymbol{\omega}_i, \alpha) = \frac{\hat{\boldsymbol{n}} \cdot \boldsymbol{\omega}_i}{(\hat{\boldsymbol{n}} \cdot \boldsymbol{\omega}_i)(1 - k) + k} \qquad (27)$$

where α is the parameter indicating surface roughness, k is a parameter derived from the roughness, typically calculated as $k = \frac{\alpha^2}{2}$.

B. Additional Implementation Details

B.1. Implemetaions of SIR

In Sec. 3.5, we use a three-phase training strategy to implement our overall framework, which includes the geometry and HDR radiance field, irradiance and hard shadow field, and material and soft shadow estimation. The details are as follows:

Phase 1: Geometry and HDR radiance field. We jointly optimize the geometry network f_d and HDR-radiance network f_c in this stage following VolSDF [16]. During the training process, we observe that the vanilla VolSDF method falls short in effectively reconstructing scene geometry, a shortfall that considerably hampers the enhancement of shadows and materials. Consequently, we explore the integration of supplementary constraints to address these limitations. In synthetic datasets, we enhance the VolSDF to add an extra output for predicting normals. We supervise the predicted normals $\boldsymbol{n}$ using gradient-based normal $\bar{\boldsymbol{n}}$, resulting in smoother predicted normals. In real-world datasets, the geometric performance of VolSDF significantly declines compared to synthetic datasets. Therefore, inspired by the MonoSDF [54], we integrate ground truth normal to constrain our gradient-based normal $\bar{\boldsymbol{n}}$. and the ground truth normal is predicted by [55]. We optimize our geometry and HDR-radiance network for 250k iterations with a batch size of 1024 in this stage, which takes about 15 hours for a scene.

Phase 2: Hard shadow and irradiance field. For the representation of irradiance I_{ir} and hard shadow S_{hard}, we

use two separate MLPs, each consisting of 4 layers of 256 hidden units with a rectified linear unit (ReLU) activation function. In addition, we encode the input surface position $\hat{\mathbf{x}}$ with 10 levels of periodic functions, respectively, before feeding them into our network. We use the incoming diffuse lighting $L_{i,d}$ in Sec. 3.2 and hard shadow ξ in Sec. 3.3 as the pseudo-GT to supervise the predicted irradiance I_{ir} and hard shadow S_{hard} via ℓ_1 loss. We use 512 sample directions over hemisphere Ω^+ to precompute the diffuse lighting $L_{i,d}$ and hard shadow ξ at sampled surface points. We set the threshold μ as 4 in synthetic scenes and 3 in real-world scenes to obtain the hard shadow ξ by distinguishing HDR radiance intensity between the main light and environment light. We optimize our irradiance and hard shadow MLPs for 10k iterations with a batch size of 256 in this stage, which takes about 7 hours for a scene.

Phase 3: BRDF and soft shadow field. In the section of material estimation (Sec. 3.4), the BRDF MLPs include four fully connected layers, each with 512 hidden units and ReLU activation functions. Following these four layers, the BRDF feature network is divided into separate albedo and roughness layers with 512 hidden units and Sigmoid activation. Specifically, albedo layer outputs the albedo term $\hat{A} \in \mathbb{R}^3$ and roughness layer outputs the roughness term $\hat{R} \in \mathbb{R}^1$ at surface position $\hat{\mathbf{x}}$. We use 64 sample directions (8×16) over hemisphere Ω^+ at sampled surface points for the specular environment map, and then when we use the specular environment map as specular incoming lighting with specular BRDF term f_s to compute the rendering equation. We use an important sampling method to sample the incoming light radiance by interpolating the specular environment map based on nvdiffrast [56], the important sampling number is 128.

For the training strategy of material estimation, we first freeze the final roughness layer and shadow term from the hard shadow MLP Θ_h and optimize the BRDF layer and albedo layer based on the diffuse component $L_{o,d}$ to obtain a coarse albedo with residual shadow. Next, we optimize the soft shadow MLP Θ_s and the albedo while keeping the roughness layer fixed. Here, the initial network parameters of the soft shadow MLP are inherited from the hard shadow MLP, providing a reasonable initial value to facilitate faster network convergence. Finally, we use instance-level albedo and roughness regularization while keeping the soft shadow MLP parameters fixed. For real-world datasets, we obtain the instance mask using the SegAny model [57]. In this stage, we optimize our BRDF model for 25K iterations with a batch size of 256, which takes approximately 25 hours for a single scene. We set weights $\lambda_{eik} = 0.1$, $\lambda_{normal} = 0.001$, $\lambda_{albedo} = 0.0003$, $\lambda_{rough} = 0.001$ in our experiments.

B.2. Implemetaions of Baselines

As shown in Table 1 and Fig. 3, we selected four prominent and widely acknowledged inverse rendering methods as our baselines: 1) NVDIFFREC [12], 2) IBL-NeRF [36], 3) PhySG [32], and 4) InvRender [33]. While TexIR [37], a recent notable approach for indoor inverse rendering using multi-view images, was also considered. However, due to its focus on large indoor scenes, which is incompatible with our dataset, it was excluded from our experimental baseline. Additionally, NeRFactor [58], a pioneering work in multi-view neural inverse rendering, was not included as a baseline in our study, given its comprehensive prior evaluation in InvRender [33]. Considering that our method incorporates additional normal constraints to improve geometric reconstruction, we make specific adjustments to ensure fairness in comparison. For synthetic datasets, we introduce a normal smooth loss, while for real-world scene datasets, we include normal ground truth supervision. To maintain consistency, we modify the geometric modules of PhySG [32] and In-vRender [33], both of which are also based on SDF-based methods, to align with our approach. However, due to challenges in adapting IBL-NeRF [36] and NVDIFFREC [12] to match our geometric framework, we provide normal ground truth as geometric supervision for these methods.

C. Details of Experiments

C.1. Additional Results on Synthetic Dataset

We present additional qualitative (see Fig. 6 and 7) and quantitative (see Table 5, 6, 7, 8, 9, 10, and 11) comparison results on the synthetic dataset including 6 scenes. Compared to other inverse rendering methods, our approach excels in estimating albedo. Crucially, it effectively separates shadows and ensures that they are not incorrectly included in the albedo, especially under indoor lighting conditions. Note that PhySG [32] and InvRender [33] directly use our trained SDF-based radiance field as their geometry backbone. Since the predicted roughness of PhySG is global, it cannot converge on our indoor scene dataset. Therefore, we ignore the comparison of the roughness MSE metric with PhySG.

C.2. Additional Results on Real Dataset

Our comparative analysis on the real-world dataset, constrained to view synthesis metrics due to the unavailability of real scene material ground truths, is presented in Table **??**. Although our method is slightly inferior to IBL-NeRF in terms of PSNR, it significantly outperforms other methods regarding SSIM and LPIPS metrics. Fig. 8 provides additional qualitative results that highlight our exceptional decomposition ability. We effectively disentangle albedo and shadow components, achieving physical plausibility in our results.

C.3. Additional Results for Ablation studies

We showcase the effectiveness of our material optimization on synthetic datasets in Table 12, 13, 14, 15, 16, 17, 18, and 19. As described in Sec. 4.4 in the main paper, Without shadow terms significantly impacts albedo estimation, leading to incorrect albedo outputs that erroneously incorporate baked shadows; Without the soft shadow term, residual shadows remain baked into the albedo, and due to the binary nature of hard shadows, they fail to accurately represent physically plausible shadow elements; Without the incorporation of an instance-level albedo regularizer, there would likely be a lack of illumination consistency in the albedo for individual instances, potentially leading to less accurate synthesis results. We show more qualitative results in Fig. 9 and 10.
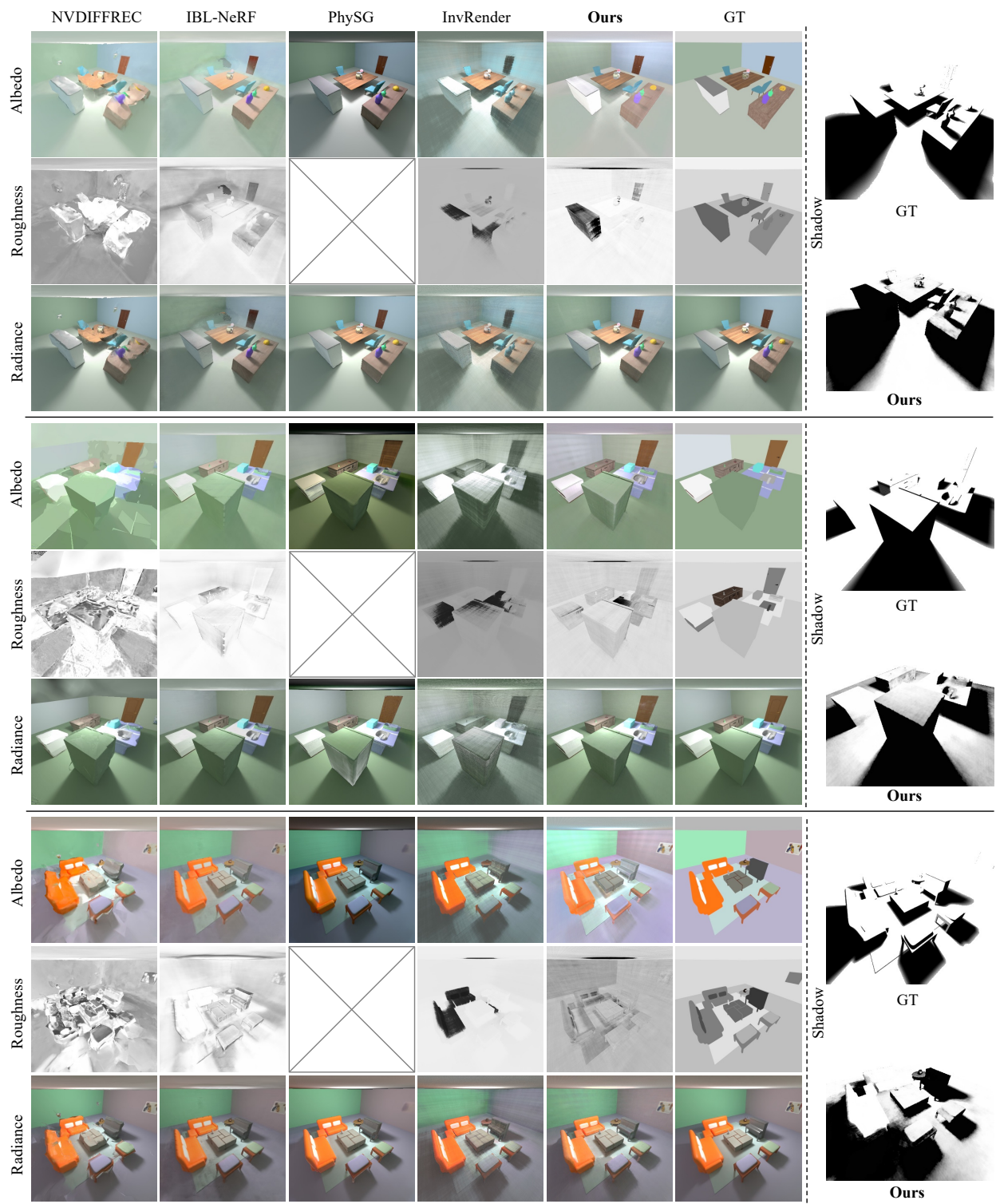
Figure 6. Qualitative results of all methods on the synthetic dataset (*Dinning*, *Kitchen*, and *Reception*).

Figure 7. Qualitative results of all methods on the synthetic dataset (*Study Room*).

Figure 8. Qualitative results of all methods on the real-world dataset (*Dinning*).

Table 4. All scores on *View Synthesis* of all baselines and our method on 2 scenes of real-world dataset.

| | PSNR↑ | | | SSIM↑ | | | LPIPS↓ | | |
	Dinning	Office	Avg.	Dinning	Office	Avg.	Dinning	Office	Avg.
NVDIFFREC [12]	21.3349	**24.0942**	22.7146	0.7480	0.8116	0.7798	0.4686	0.4226	0.4456
IBL-NeRF [36]	**26.234**	22.3221	**24.2781**	0.7968	0.7013	0.7491	0.4285	0.6165	0.5225
PhySG [32]	23.1329	21.1654	22.1492	0.7837	0.7755	0.7796	0.4871	0.4290	0.4581
InvRender [33]	21.3901	18.8752	20.1327	0.7025	0.6364	0.6694	0.6436	0.6331	0.6384
SIR (Ours)	23.7331	21.9021	22.8176	**0.8272**	**0.8418**	**0.8345**	**0.2854**	**0.3007**	**0.2931**

Figure 9. Qualitative results of ablation study on the synthetic dataset (*left: Bathroom, right: Dinning*).

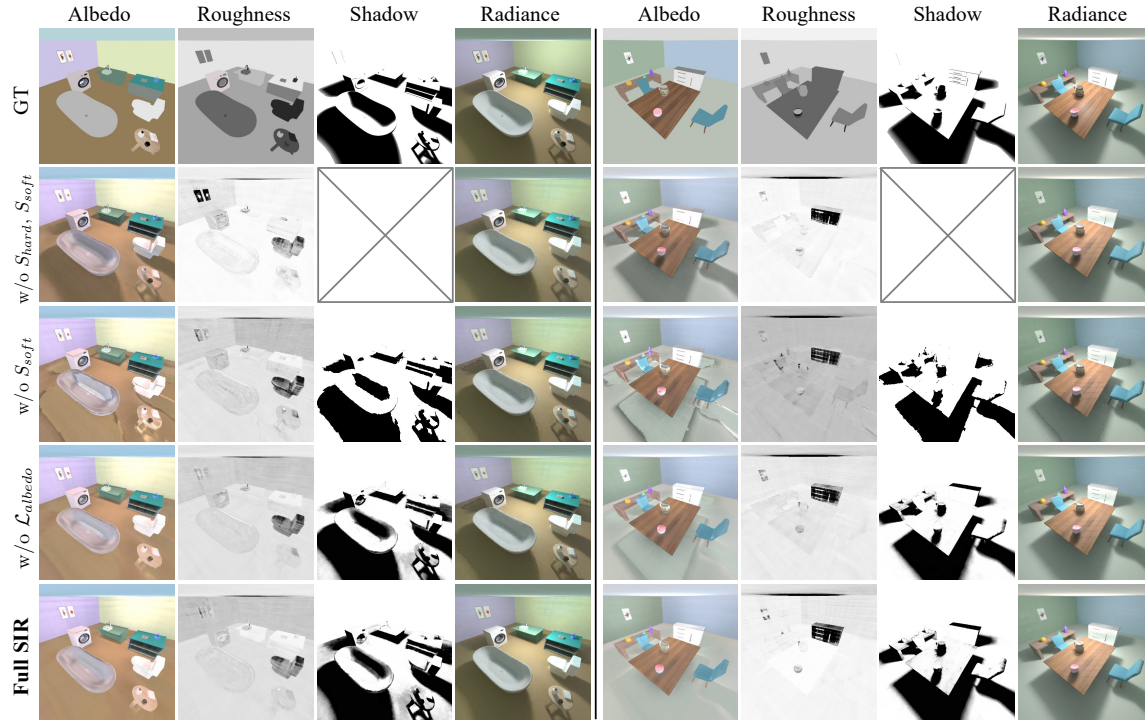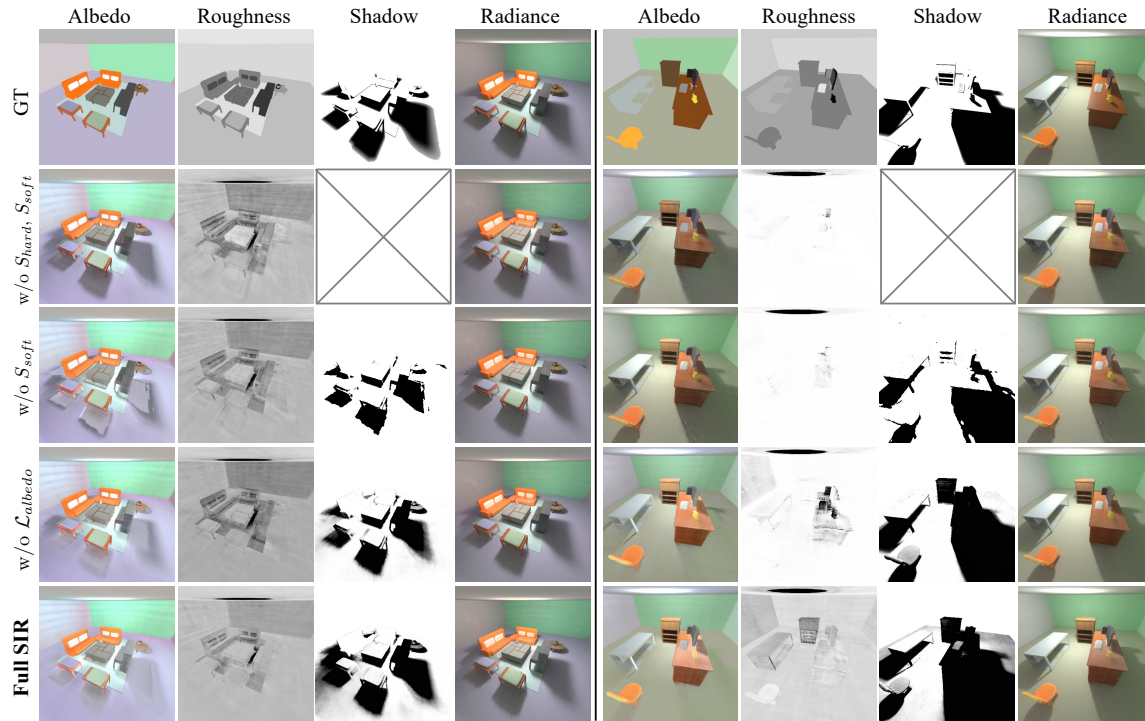Figure 10. Qualitative results of ablation study on the synthetic dataset (*left: Reception, right: Study Room*).

Table 5. PSNR↑ scores on *Albedo* of all baselines and our method on 6 scenes of synthetic dataset.

	Bathroom	Dinning	Kitchen	Reception	Restroom	Study Room	Avg.
NVDIFFREC [12]	16.5426	16.9962	16.9461	15.8834	15.8183	17.6397	16.6377
IBL-NeRF [36]	16.9009	17.4294	18.7986	14.9936	17.5475	14.9937	16.7773
PhySG [32]	11.9364	10.5226	9.1063	8.7889	10.7602	12.0790	10.5322
InvRender [33]	14.5135	12.4979	11.6564	11.6064	13.7893	11.1773	12.5401
SIR (Ours)	**20.5327**	**21.4604**	**20.0423**	**19.9779**	**21.3194**	**18.3272**	**20.2767**

Table 6. SSIM↑ scores on *Albedo* of all baselines and our method on 6 scenes of synthetic dataset.

	Bathroom	Dinning	Kitchen	Reception	Restroom	Study Room	Avg.
NVDIFFREC [12]	0.7809	0.7993	0.7630	0.7758	0.8046	0.8338	0.7906
IBL-NeRF [36]	0.8592	0.8425	0.8526	**0.8349**	0.8568	0.8349	0.8468
PhySG [32]	0.7472	0.7197	0.6582	0.6521	0.7261	0.7420	0.7076
InvRender [33]	0.7253	0.7068	0.6145	0.7173	0.7124	0.5678	0.6740
SIR (Ours)	**0.8654**	**0.8815**	**0.8643**	0.8293	**0.8740**	**0.8452**	**0.8600**

Table 7. LPIPS↓ scores on *Albedo* of all baselines and our method on 6 scenes of synthetic dataset.

	Bathroom	Dinning	Kitchen	Reception	Restroom	Study Room	Avg.
NVDIFFREC [12]	0.4326	0.3260	0.4615	0.3355	0.3657	0.3201	0.3736
IBL-NeRF [36]	0.2360	0.2451	0.2474	0.2545	**0.2469**	0.2545	0.2161
PhySG [32]	0.3275	0.3572	0.3953	0.4886	0.3820	0.3524	0.3838
InvRender [33]	0.4089	0.4669	0.6359	0.4416	0.5083	0.4996	0.4935
SIR (Ours)	**0.2064**	**0.1560**	**0.2124**	**0.2155**	0.2599	**0.2420**	**0.2154**

Table 8. MSE↓ scores on *Roughness* of all baselines and our method on 6 scenes of synthetic dataset.

	Bathroom	Dinning	Kitchen	Reception	Restroom	Study Room	Avg.
NVDIFFREC [12]	0.0725	0.0620	0.0454	0.0450	0.0419	0.0515	0.0531
IBL-NeRF [36]	0.0824	0.0520	**0.0334**	0.0507	0.0691	0.0507	0.0564
PhySG [32]	-	-	-	-	-	-	-
InvRender [33]	**0.0325**	**0.0240**	0.0373	0.0470	0.0691	0.0455	**0.0412**
SIR (Ours)	0.0547	0.0667	0.0408	**0.0278**	**0.0318**	**0.0451**	0.0445

Table 9. PSNR↑ scores on *View Synthesis* of all baselines and our method on 6 scenes of synthetic dataset.

	Bathroom	Dinning	Kitchen	Reception	Restroom	Study Room	Avg.
NVDIFFREC [12]	25.0672	22.9778	21.7287	23.5271	24.0889	25.4392	23.8048
IBL-NeRF [36]	26.1249	24.2538	25.3530	23.1610	25.1013	23.1610	24.5258
PhySG [32]	28.5612	28.9428	18.9739	26.0657	28.7668	25.6900	26.1667
InvRender [33]	26.1792	26.5549	13.9339	25.8879	25.8880	24.7052	23.8582
SIR (Ours)	**28.9697**	**29.0003**	**30.1561**	**26.7210**	**29.4958**	**26.9309**	**28.5456**

Table 10. SSIM↑ scores on *View Synthesis* of all baselines and our method on 6 scenes of synthetic dataset.

	Bathroom	Dinning	Kitchen	Reception	Restroom	Study Room	Avg.
NVDIFFREC [12]	0.8799	0.8340	0.8303	0.8530	0.9152	0.9059	0.8606
IBL-NeRF [36]	**0.9379**	0.9072	0.8303	**0.9273**	**0.9338**	0.9273	**0.9263**
PhySG [32]	0.9352	**0.9383**	0.8676	0.9189	0.9336	**0.9278**	0.9202
InvRender [33]	0.8054	0.7863	0.5798	0.8370	0.8370	0.7523	0.7521
SIR (Ours)	0.9276	0.9329	**0.9267**	0.9152	0.9279	0.9244	0.9258

Table 11. LPIPS↓ scores on *View Synthesis* of all baselines and our method on 6 scenes of synthetic dataset.

	Bathroom	Dinning	Kitchen	Reception	Restroom	Study Room	Avg.
NVDIFFREC [12]	0.1771	0.2163	0.2391	0.1699	0.1832	0.1294	0.1863
IBL-NeRF [36]	**0.0679**	0.1250	**0.0710**	**0.0790**	**0.0592**	**0.0790**	**0.0844**
PhySG [32]	0.0756	0.0829	0.1760	0.1104	0.0770	0.0865	0.1014
InvRender [33]	0.3047	0.3594	0.6263	0.2788	0.3022	0.3678	0.3923
SIR (Ours)	0.0916	**0.0778**	0.0949	0.1044	0.1158	0.0940	0.0964

Table 12. PSNR↑ scores on *Albedo* of ablation study on 6 scenes of synthetic dataset.

	Bathroom	Dinning	Kitchen	Reception	Restroom	Study Room	Avg.
(1) w/o S_{hard}, S_{soft}	20.1723	17.7693	16.2957	16.9954	13.1248	15.4890	16.6411
(2) w/o S_{soft}	20.6228	**22.0081**	18.7957	19.5625	16.7769	**18.5355**	19.3836
(3) w/o $\mathcal{L}_{albedo}$	**20.7954**	21.2082	19.5987	19.8224	16.6736	17.4599	19.2597
Full SIR	20.5327	21.4604	**20.0423**	**19.9779**	**21.3194**	18.3272	**20.2767**

Table 13. SSIM↑ scores on *Albedo* of ablation study on 6 scenes of synthetic dataset.

	Bathroom	Dinning	Kitchen	Reception	Restroom	Study Room	Avg.
(1) w/o S_{hard}, S_{soft}	0.8340	0.8314	0.8161	0.7935	0.7756	0.7998	0.8084
(2) w/o S_{soft}	0.8249	0.8310	0.8258	0.7925	0.7536	0.8035	0.8052
(3) w/o $\mathcal{L}_{albedo}$	0.8628	0.8713	0.8598	0.8183	0.8349	0.8255	0.8454
Full SIR	**0.8654**	**0.8815**	**0.8643**	**0.8293**	**0.8740**	**0.8452**	**0.8600**

Table 14. LPIPS↓ scores on *Albedo* of ablation study on 6 scenes of synthetic dataset.

	Bathroom	Dinning	Kitchen	Reception	Restroom	Study Room	Avg.
(1) w/o S_{hard}, S_{soft}	0.2629	0.2541	0.2904	0.2649	0.3366	0.3423	0.2919
(2) w/o S_{soft}	0.2806	0.2650	0.2936	0.2717	0.3676	0.3580	0.3061
(3) w/o $\mathcal{L}_{albedo}$	0.2187	0.1888	0.2293	0.2324	0.2686	0.3059	0.2406
Full SIR	**0.2064**	**0.1560**	**0.2124**	**0.2155**	**0.2599**	**0.2420**	**0.2154**

Table 15. MSE↓ scores on *Roughness* of ablation study on 6 scenes of synthetic dataset.

	Bathroom	Dinning	Kitchen	Reception	Restroom	Study Room	Avg.
(1) w/o S_{hard}, S_{soft}	**0.0300**	0.0719	0.0901	0.0343	0.0824	0.1187	0.2919
(2) w/o S_{soft}	0.0542	**0.0247**	0.0613	0.0300	0.0863	0.1194	0.3061
(3) w/o $\mathcal{L}_{albedo}$	0.0526	0.0506	0.0736	0.0372	0.0836	0.1078	0.2406
Full SIR	0.0547	0.0667	**0.0408**	**0.0278**	**0.0318**	**0.0451**	**0.2154**

Table 16. MSE↓ scores on *Shadow* of ablation study on 6 scenes of synthetic dataset.

	Bathroom	Dinning	Kitchen	Reception	Restroom	Study Room	Avg.
(1) w/o S_{hard}, S_{soft}	-	-	-	-	-	-	-
(2) w/o S_{soft}	0.0513	0.0485	0.0503	**0.0645**	0.0752	0.1004	0.0650
(3) w/o $\mathcal{L}_{albedo}$	0.0599	0.0764	0.0667	0.1026	0.0768	0.1354	0.0863
Full SIR	**0.0253**	**0.0475**	**0.0350**	0.1086	**0.0520**	**0.0560**	**0.0541**

Table 17. PSNR↑ scores on *View Synthesis* of ablation study on 6 scenes of synthetic dataset.

	Bathroom	Dinning	Kitchen	Reception	Restroom	Study Room	Avg.
(1) w/o S_{hard}, S_{soft}	28.4005	28.8354	28.6415	26.9213	**29.6099**	26.9436	28.2254
(2) w/o S_{soft}	28.4757	29.0484	29.2856	26.7187	26.9242	26.4678	27.8201
(3) w/o $\mathcal{L}_{albedo}$	28.8861	**29.5537**	28.9922	**26.9596**	28.5293	**27.2453**	28.3610
Full SIR	**28.9697**	29.0003	**30.1561**	26.7210	29.4958	26.9309	**28.5456**

Table 18. SSIM↑ scores on *View Synthesis* of ablation study on 6 scenes of synthetic dataset.

	Bathroom	Dinning	Kitchen	Reception	Restroom	Study Room	Avg.
(1) w/o S_{hard}, S_{soft}	0.9226	0.9288	0.9242	0.9160	0.9277	0.9134	0.9221
(2) w/o S_{soft}	0.9058	0.9070	0.9076	0.9013	0.8490	0.8968	0.8946
(3) w/o $\mathcal{L}_{albedo}$	0.9267	0.9322	**0.9275**	0.9145	0.9277	**0.9260**	**0.9258**
Full SIR	**0.9276**	**0.9329**	0.9267	**0.9152**	**0.9279**	0.9244	**0.9258**

Table 19. LPIPS↓ scores on *View Synthesis* of ablation study on 6 scenes of synthetic dataset.

	Bathroom	Dinning	Kitchen	Reception	Restroom	Study Room	Avg.
(1) w/o S_{hard}, S_{soft}	0.0996	0.0828	0.0955	0.1049	**0.0832**	0.1185	0.0974
(2) w/o S_{soft}	0.1616	0.1839	0.1587	0.1656	0.2706	0.1980	0.1897
(3) w/o $\mathcal{L}_{albedo}$	0.0944	0.0811	**0.0913**	0.1089	0.0851	**0.0936**	**0.0924**
Full SIR	**0.0916**	**0.0778**	0.0949	**0.1044**	0.1158	0.0940	0.0964